ELSEVIER

Contents lists available at ScienceDirect

# **Materials Today Physics**

journal homepage: https://www.journals.elsevier.com/ materials-today-physics



# Quasi-1D electronic transport and isotropic phonon transport in the Zintl Ca<sub>5</sub>In<sub>2</sub>Sb<sub>6</sub>



David M. Smiadak <sup>a</sup>, Romain Claes <sup>b</sup>, Nicolas Perez <sup>c</sup>, Mack Marshall <sup>a</sup>, Wanyue Peng <sup>a</sup>, Wei Chen <sup>b</sup>, Geoffroy Hautier <sup>b, d</sup>, Gabi Schierning <sup>c, e</sup>, Alexandra Zevalkink <sup>a, \*</sup>

- <sup>a</sup> Department of Chemical Engineering and Materials Science, Michigan State University, East Lansing, MI, 48 824, USA
- b Institute of Condensed Matter and Nanosciences, Université Catholique de Louvain, Chemin des Étoiles 8, 1348, Louvain-la-Neuve, Belgium
- <sup>c</sup> Leibniz Institute for Solid State and Material Research Dresden (IFW Dresden), 01 069, Dresden, Germany
- <sup>d</sup> Thayer School of Engineering, Dartmouth College, Hanover, NH, 03 755, USA
- <sup>e</sup> Experimental Physics, Bielefeld University, 33 615, Bielefeld, Germany

#### ARTICLE INFO

# Article history: Received 27 July 2021 Received in revised form 6 December 2021 Accepted 20 December 2021 Available online 5 January 2022

Keywords:
Zintl phases
Lithography
Crystal structure
Electronic structure
Single crystal X-ray diffraction
Thermoelectrics
Flux growth

#### ABSTRACT

Crystals with anisotropic thermoelectric transport coefficients can yield a high figure-of-merit along the direction with the highest electronic mobility, provided the Seebeck coefficient and thermal conductivity are relatively isotropic. In this study, we combine experiment and theory to investigate the anisotropic properties of the quasi-1D Zintl phase Ca<sub>5</sub>In<sub>2</sub>Sb<sub>6</sub>. Ca<sub>5</sub>In<sub>2</sub>Sb<sub>6</sub> is predicted by *ab initio* calculations to have extremely anisotropic p-type electrical conductivity and power factor, arising from light effective mass parallel to its ladder-like polyanionic chains. In contrast, the Seebeck coefficient and lattice thermal conductivity are predicted to be relatively isotropic. The latter is evidenced by the nearly isotropic computed speed of sound tensor and experimentally obtained thermal expansion coefficients. In order to characterize the anisotropic electrical conductivity, Ca<sub>5</sub>In<sub>2</sub>Sb<sub>6</sub> single crystals were grown from an In-Sb rich molten flux and measured both parallel and perpendicular to the polyanionic chains. Due to the small crystal cross-sections, measurements perpendicular to the growth direction demanded a novel photolithography methodology whereby micro-ribbons were extracted using focused ion beam milling, and processed using laser photolithography to deposit contacts for electrical resistivity and Hall coefficient measurements. The conductivity parallel to the growth direction was found to be nearly 20x higher than the perpendicular direction, in agreement with our theoretical predictions. This study represents one of the first experimental confirmations of highly anisotropic electrical conductivity in Zintl thermoelectrics.

© 2021 Elsevier Ltd. All rights reserved.

# 1. Introduction

Thermoelectric materials, used to convert heat into electricity, have a wide variety of applications including industrial waste-heat recovery, remote sensing, and powering space exploration [1]. High efficiency thermal-to-electrical energy conversion requires materials with a high Seebeck coefficient and electrical conductivity while possessing low thermal conductivity. This combination is exceptionally difficult to achieve simultaneously — posing a fundamental dilemma for those developing materials with improved thermoelectric figure-of-merit (*zT*). Materials with

these properties, since the degree of anisotropy exhibited by each transport coefficient can differ [2,3]. This has been demonstrated in several important thermoelectric materials [3–5], including the recent study of single crystalline SnSe, in which exceptionally high zT values (> 2) were reported [2]. In all of these cases, the highest zT is found to be in the direction with the highest electrical conductivity.

anisotropic crystal structures offer a potential strategy to decouple

Zintl phases, with their vast range of structural patterns in noncubic space groups [6] and their excellent high-temperature thermoelectric performance [7], stand out as an intriguing area for transport anisotropy studies. The covalently-bonded polyanions exemplified by Zintl phases crystallize in a diverse range of highly anisotropic sub-structures, including isolated moieties (*e.g.*, Yb<sub>14</sub>MnSb<sub>11</sub> [8]), 1D chains (A<sub>5</sub>M<sub>2</sub>Sb<sub>6</sub> and A<sub>3</sub>MSb<sub>3</sub>), 2D sheets

E-mail address: alexzev@msu.edu (A. Zevalkink).

<sup>\*</sup> Corresponding author.

(AM<sub>2</sub>X<sub>2</sub> [9]) and 3D networks (KGaSb<sub>4</sub> [10], BaGa<sub>2</sub>Sb<sub>2</sub> [11]). However, despite ample theoretical evidence [12–15] of light effective mass and enhanced thermoelectric efficiency in the covalentlybonded direction, experimental confirmation is still lacking in the vast majority of Zintl compounds. This knowledge gap has been exacerbated by the difficulty of growing single crystals of sufficient size and quality for complete transport property characterization. Zintl compounds often melt incongruently, have high melting temperatures, and contain reactive and/or high vapor-pressure elements, all of which make directional solidification methods (e.g., Bridgman or Czochralski techniques) impractical. Zintl crystals are usually precipitated from a molten metal flux [16], which has the advantage of reducing the melting temperature, diluting the most reactive elements (usually the cation), and allowing for growth of incongruent phases. The drawback is often small, anisotropic crystals with at least one difficult-to-characterize dimension.

In this study, we combine theory and experiment to investigate the anisotropic behavior of the quasi-1D compound, Ca<sub>5</sub>In<sub>2</sub>Sb<sub>6</sub>. The structure of Ca<sub>5</sub>In<sub>2</sub>Sb<sub>6</sub>, shown in Fig. 1(a), is characterized by anionic sub-structures (Fig. 1(b)) resembling chains of cornerlinked InSb4 tetrahedra aligned in the c-direction. Each neighboring chain is joined via Sb-Sb covalent bonds to form infinite polyanionic ladders. Prior computational studies have predicted highly anisotropic effective mass, with light effective mass in the cdirection, but this has not been confirmed experimentally [12]. Instead, prior experimental studies of the A<sub>5</sub>M<sub>2</sub>Sb<sub>6</sub> family of compounds (including A = Ca, Sr, and M = Al, Ga, In) have focused on optimizing composition through doping and alloying, leading to promising zT values at intermediate temperatures (e.g., zT = 0.7 in Zn-doped Ca<sub>5</sub>In<sub>2</sub>Sb<sub>6</sub> at 900 K) in polycrystalline samples [17]. Here, we revisit ab initio predictions of anisotropic electronic properties using an improved scattering model and we investigate thermal anisotropy using ab-initio phonon calculations and experimental thermal expansion coefficients. We employ a photolithography approach to measure electronic transport along the smallest dimension of Ca<sub>5</sub>In<sub>2</sub>Sb<sub>6</sub> crystals grown from molten metal flux, allowing us to obtain electrical resistivity both parallel and perpendicular to the growth direction for the first time.

# 2. Methods

Synthesis: First, polycrystalline Ca<sub>5</sub>In<sub>2</sub>Sb<sub>6</sub> was synthesized as a precursor by using stoichiometric quantities of high-purity Ca (dendritic pieces, Sigma-Aldrich 99.9%), In (shot, Alfa Aesar 99.9995%), and Sb (shot, Alfa Aesar 99.999%), which were then milled in a SPEX MixerMill 8000D in 5 g batches, under argon atmosphere using two 12.7 mm stainless steel balls for 60 min. The resulting powder was loaded into 10 mm graphite dies (POCO EDM-3) with graphite foil spacers. Samples were spark plasma sintered in a Dr. Sinter 211LX system under vacuum using a heating profile of room temperature to 823 K in 5 min and maintained at temperature for 10 min, achieving phase-pure polycrystalline precursor. Single crystals were grown using the self-flux method. Polycrystalline Ca<sub>5</sub>In<sub>2</sub>Sb<sub>6</sub> samples were loaded with In-Sb flux at a ratio of Ca<sub>5</sub>In<sub>2</sub>Sb<sub>6</sub> to In<sub>73</sub>Sb<sub>42</sub> flux into Canfield crucibles [18] and sealed in quartz ampules under vacuum. Ampules were heated to 1173 K in 12 h, maintained at 1173 K for 2 h and then cooled slowly to 1003 K at 3 K/h. Ampules were then extracted from the furnace and centrifuged at 2500 RPM for 2 min to separate the liquid flux from the Ca<sub>5</sub>In<sub>2</sub>Sb<sub>6</sub> crystals.

**Morphology and phase analysis:** Scanning electron microscopy (SEM) was performed using a Zeiss Evo LS25, and a Tescan Mira 3XMH. An EDAX Apollo X module was used for energy-dispersive X-ray spectroscopy (EDS) to determine the approximate chemical composition. Single crystal X-ray diffraction was performed to

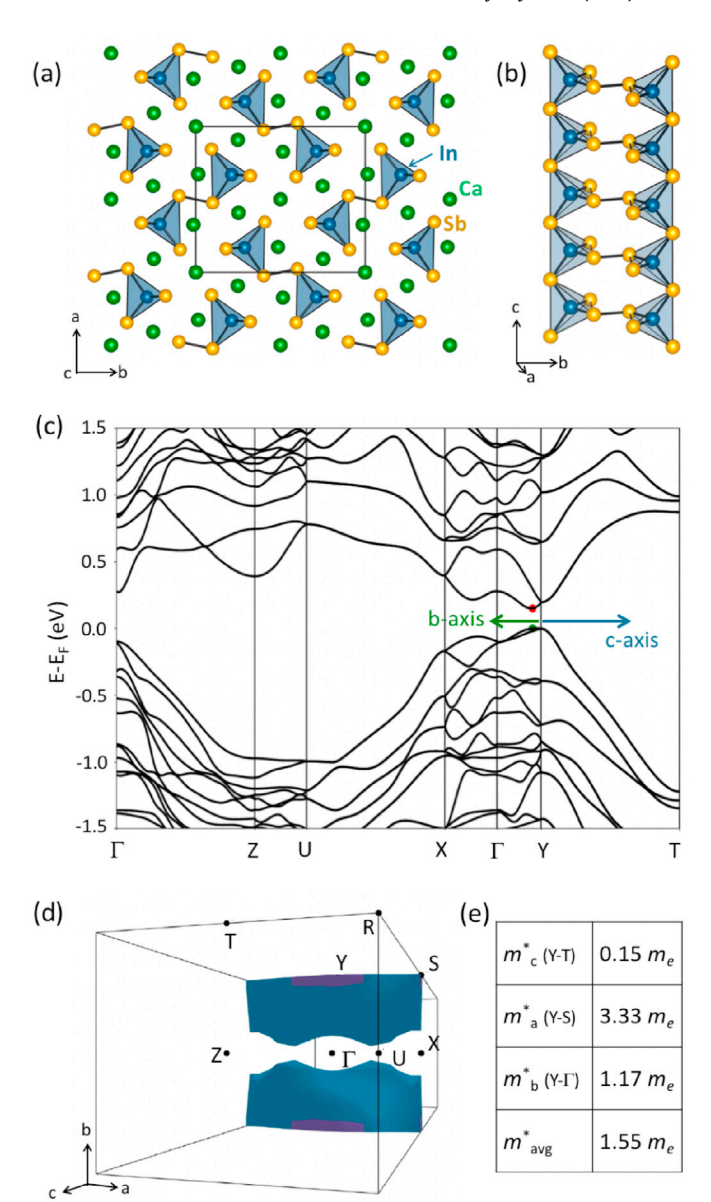


**Fig. 1.** (a) The orthorhombic unit cell of  $Ca_5In_2Sb_6$  contains (b) 1D tetrahedral ladders aligned parallel to the c-axis. (c) The electronic band structure has a direct band gap with valence band maximum between  $\Gamma$  and  $\Upsilon$  consisting of two degenerate bands. (d) The Fermi surface of  $Ca_5In_2Sb_6$  at a hole concentration of  $1 \times 10^{19} \ h^+/cm^3$  reveals quasi-1D conduction (e) with light conductivity effective mass in the c-direction, parallel to the ladders, and heavier mass in the a- and b-directions.

confirm the crystal structure and orient the crystals. A Bruker-AXS Apex II CCD instrument was used at 173 K under a cold nitrogen stream, with reflection data acquired using a graphite-monochromated Mo-K $\alpha$  radiation source ( $\lambda = 0.710~73~\text{Å}$ ) producing a 0.5 mm beam diameter. Data was integrated with SAINT [19]. Structures were solved using direct methods and refined on  $F^2$  using SHELX [20] subroutines within the Olex2-1.2 crystallographic suite [21]. Reflections were merged using SHELXL [22].

**Thermal expansion:** High temperature powder X-ray diffraction was performed using a Rigaku Smartlab X-ray diffraction system with  $Cu-K\alpha$  radiation, equipped with a Rigaku HT1500 high-temperature stage. Samples were ground into fine powders and placed on a platinum tray. Measurements were performed under vacuum to prevent oxidation. The heating and cooling rate was

10 K/min with a 1 min hold, and sample height alignments were performed before each scan to account for the thermal expansion of both the holder and sample. Lattice parameters were obtained via Rietveld refinement using PDXL2 software and showed no hysteresis between heating and cooling.

Photolithography: To measure electronic properties perpendicular to the growth direction, a micro-photolithography process was developed. Ca<sub>5</sub>In<sub>2</sub>Sb<sub>6</sub> micro-ribbons with dimensions in the range of  $18-80 \times 3-7 \times 0.2-0.5 \mu m$  were extracted from individual crystals using a focused ion beam (FIB) equipped FEI Helios Nano-Lab 600i EDS instrument with crystal composition confirmed locally by EDS prior to milling. FIB cutting was conducted with a milling voltage and current of 30 kV/65 nA respectively, with smaller currents (as low as 80 pA) used for thinning and milling of the edges. The micro-ribbons were then transferred onto glass substrates. Ti Prime and image reversal photoresist AZ 5214 E was applied using Polos spin coaters with soft/hard bakes performed on hot plates. Laser lithography was conducted on a  $\mu$ -PG 101 micro pattern generator manufactured by Heidelberg Instruments using a 375 nm laser. The circuit was designed from a digital photomask in LASI7 and consisted of two thermocouples, two dedicated current lines, a Hall sensor, and a heater [23]. Flood exposures occurred in a custom stand-alone unit using 375 nm light. After development, photoresist quality was evaluated with a Bruker DektakXT stylus profiler. Sputter deposition of a 50 nm thick Cr adhesion layer and a 200 nm thick primary Au layer was accomplished using a Compact Research Coater (CRC-622-2G2-RF-DC) magnetron sputtering system manufactured by Torr International, Lift-off occurred using a standard remover in a petri dish on a hot plate at 80 °C to expedite the process. Additional processing details can be found in ref. [24].

**Transport measurements:** Electrical transport characterization of micro-ribbons was conducted on a Quantum Design Dynacool cryostat with a 14 T magnet. Resistance was characterized using a sourcemeter Keithley 2400 and a nanovoltmeter Keithley 2182 A. Samples were mounted to Quantum Design Physical Property Measurement System (PPMS) pucks with GE varnish and bonded to external contact pads with 25  $\mu$ m Au wire using a TPT HB16 semi-automatic bonder.

Electrical resistivity measurements of  $5-10~\mathrm{mm}$  crystals along the preferred growth direction (parallel to c-direction) were carried out using a custom-built cryostat system based on a standard four-terminal resistance configuration. Electrical contacts were made with Pelco colloidal silver liquid (Ted Pella) and insulated single strand Cu wire (dia.  $= 0.07~\mathrm{mm}$ ).

Computational details: The electronic structure of Ca<sub>5</sub>In<sub>2</sub>Sb<sub>6</sub> was computed using density functional theory (DFT) and the Vienna ab initio Simulation Package (VASP) [25] using the Perdew-Burke-Ernzerhof (PBE) generalized gradient approximation (GGA) [26], the projector augmented-wave (PAW) approach [27,28] and a **k**-point grid of 10x4x2. Including spin orbit coupling (SOC) was found to reduce the band gap (see Fig. S1). GW calculations using the  $G_0W_0$  method [29] were used to confirm that the band edge curvature from PBE was accurate. Details of the G<sub>0</sub>W<sub>0</sub> calculations and the resulting band structure are shown in Fig. S2 and Fig. S3. The conductivity effective masses and transport properties (obtained from PBE without SOC) were obtained with the BOLTZTRAP software [30] by solving the Boltzmann transport equation, and the Pymatgen software was used for the post-processing analysis [31]. Typically, BOLTZTRAP employs the constant relaxation time approximation for electron scattering. In order to overcome this rather rough approximation, the BOLTZTRAP software was modified to include an energy and temperature dependent relaxation time  $\tau(\epsilon,$ T) following [32]:

$$\tau(\epsilon, T) = \tau_0(\epsilon_0, T_0) \left(\frac{T}{T_0}\right)^s \left(\frac{\epsilon}{\epsilon_0}\right)^{r-1/2} \tag{1}$$

where the reference relaxation time,  $\tau_0$ , is kept variable in order to fit experimental results. The energy,  $\epsilon_0$ , and the temperature,  $T_0$ , are fixed to 0.01 eV and 600 K respectively. Parameters s and r depend on the scattering type considered. Ionized impurity (II) scattering sets the parameters to s=0 and r=2 whereas the acoustic phonon (AP) scattering use s=-1 and r=0. The contributions from the two scattering mechanisms were summed via Matthiessen's rule. Note that polar optical phonon scattering (POP) was also considered (s=-1 and r=1), but we found that the ratio of AP-to-POP did not significantly change the temperature dependence of transport coefficients. For this reason, POP was omitted for the purpose of this study.

In addition, the calculated phonon dispersion of  $Ca_5In_2Sb_6$  was obtained using density functional perturbation theory (DFPT) within the ABINIT software [33,34]. The mode Grüneisen parameters were obtained by performing calculations with a cell volume 1% larger than the initial phonon calculation and another with a volume 1% smaller. The phonon dispersion and the mode Grüneisen parameters are shown in Fig S6 and S7, respectively, together with additional details of the calculation approach.

#### 3. Results

# 3.1. Electronic structure

The electronic band structure of Ca<sub>5</sub>In<sub>2</sub>Sb<sub>6</sub>, shown in Fig. 1(c) along high symmetry directions, has a direct band gap of 0.15 eV between *Y* and Γ. Since DFT with GGA is known to underestimate band gaps, for the purposes of calculating transport coefficients, a scissor operator was used to match the experimental band gap of 0.64 eV obtained from optical measurements [12]. Below, we focus our analysis on the valence band in the energy range from  $E_F = -0.2$  to 0 eV, since, to date, all  $A_5M_2$ Sb<sub>6</sub> compounds (including A = Ca, Sr, M = Al, In, Ga) synthesized with this structure type have been p-type [35]. For Ca<sub>5</sub>In<sub>2</sub>Sb<sub>6</sub>, the nominally undoped polycrystalline samples reported in Zevalkink et al. [12], as well as the Ca<sub>5</sub>In<sub>2</sub>Sb<sub>6</sub> single crystals synthesized for the current study have n ~10<sup>18</sup> h<sup>+</sup>/cm<sup>3</sup> (corresponding to  $E_F = -0.25$  eV), while Zn-doped polycrystalline samples have been reported with up to  $10^{20}$  h<sup>+</sup>/cm<sup>3</sup> ( $E_F = -1.7$  eV).

The valence band maximum of Ca<sub>5</sub>In<sub>2</sub>Sb<sub>6</sub> consists of two bands, each of which has a degeneracy of two due to symmetry, leading to an overall band degeneracy of  $N_V = 4$ . The valence band is highly anisotropic; the Fermi surface at 10<sup>19</sup> h<sup>+</sup>/cm<sup>3</sup> resembles a plate oriented perpendicular to the c-axis (see Fig. 1(d) and Figure S4 for an additional perspective). The table shown in Fig. 1(e) compares the conductivity effective masses  $m_a^*$ ,  $m_b^*$ , and  $m_c^*$  along the three principle directions. Note that the conductivity effective mass controls electronic mobility and is determined by the average curvature of the bands near  $E_F$  in a particular k-space direction [36–38]. It takes into account all the bands and regions in the Brillouin zone involved in transport at the specified Fermi energy and temperature. The density of states effective mass  $(m_{DOS}^*)$ , in contrast, is a scalar quantity and determines the Seebeck coefficient. The distinction between  $m_{\mathrm{DOS}}^{*}$  and  $m_{i}^{*}$  is what enables enhanced zT along the light inertial mass and high mobility direction of anisotropic materials [39].

In Ca<sub>5</sub>In<sub>2</sub>Sb<sub>6</sub>, the carrier transport in the c-direction, parallel to the polyanionic chains, has the lightest mass with  $m_{c,(Y-T)}^* = 0.15$   $m_c$ , while the effective masses in the b- and a-directions are 8 and

20 times heavier, at  $m_{b,(Y-\Gamma)}^*=1.17~m_e$  and  $m_{a,(Y-S)}^*=3.33~m_e$ , respectively. The light mass in the c-direction likely stems from the polar-covalent In—Sb bonds that form a continuous chain along the c-direction. The covalent Sb—Sb dumbbells are oriented along the b-direction but do not form a continuous network. In contrast, bonding along the a-direction is characterized only by ionic Ca—Sb bonding, likely leading to the high effective mass.

A literature survey of the experimental electronic mobility of Zintl compounds supports the theory that the polyanionic substructures in Zintl phases provide channels for p-type electronic conductivity. Fig. 2 shows the intrinsic p-type mobility,  $\mu_0$ , of polycrystalline samples at 600 K as a function of an empirical constant,  $f_0 = a/(m+x)(1+\chi_X-\chi_M)$ . The first term in  $f_0$  quantifies the cation-to-anion ratio for a general composition of  $A_0M_mX_x$ . Compounds with a higher cation-to-anion ratio generally contain anionic sub-structures with a lower degree of connectivity (e.g., 1D sub-structures or isolated 0D moieties, as opposed to 2D or 3D substructures). The second term in  $f_0$  quantifies the electronegativity difference,  $\chi_X - \chi_M$ , between the M and X species that form the polvanions and thus indicates the degree of covalency in the polyanions. The strong correlation between mobility and  $f_0$  suggests that both the dimensionality and the bonding character of the polyanions are important in determining the electrical conductivity. Compounds in the Ca<sub>5</sub>M<sub>2</sub>Sb<sub>6</sub> family are thus expected to have relatively low average (i.e., polycrystalline) mobility because they have low dimensionality (1D) anionic sub-structures.

Extending the same rule-of-thumb to the single-crystal mobility of Zintl compounds, one would expect to always find the highest mobility in the real-space direction aligned parallel to the polyanions. As intuitive as this explanation appears, there are exceptions. The related compound, Ca<sub>3</sub>AlSb<sub>3</sub> [46] forms 1D polyanionic chains similar to that of Ca<sub>5</sub>In<sub>2</sub>Sb<sub>6</sub>, but its valence band is *not* predicted by DFT to be highly anisotropic. Another compound, Ba<sub>3</sub>Al<sub>2</sub>As, is actually predicted to have lighter effective mass perpendicular to its polyanionic chains [15]. This suggests that, on its own, anisotropic bonding is not a sufficient condition to yield anisotropic transport in other Zintl structure types. It is also notable that in Mg<sub>3</sub>Sb<sub>2</sub> and Mg<sub>3</sub>Bi<sub>2</sub>, the in-plane p-type conductivity is significantly lower than the out-of-plane conductivity. This has been shown both from first-principles calculations [47] and

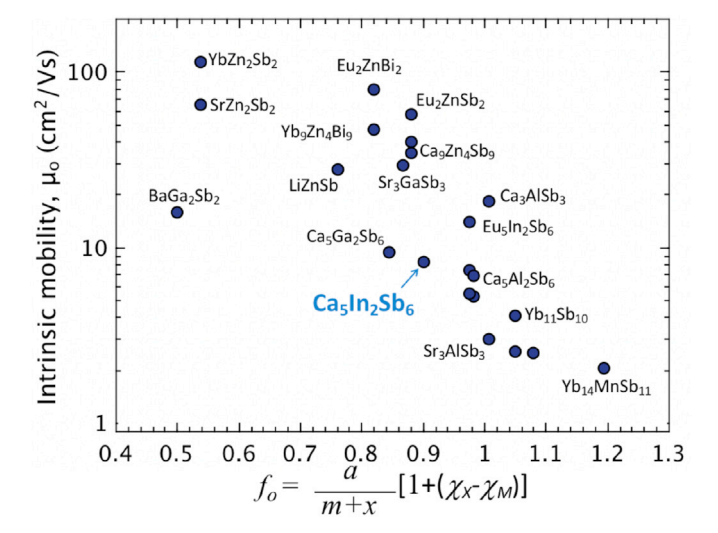


**Fig. 2.** Intrinsic mobility at 600 K in  $A_a M_m X_x$  Zintl phases was calculated from experimental Hall mobility data [8,11,12,35,40–44] using a single band model [45]. The intrinsic mobility decreases rapidly with increasing cation-to-anion ratio, a/(m+x), and electronegativity difference,  $\chi_x \gamma_M$ .

experimentally in crystals grown from flux [48]. However, since the bonding in these compounds has been shown to be a) isotropic, and b) more ionic than covalent [49], their transport properties should not be considered as representative of Zintls in general.

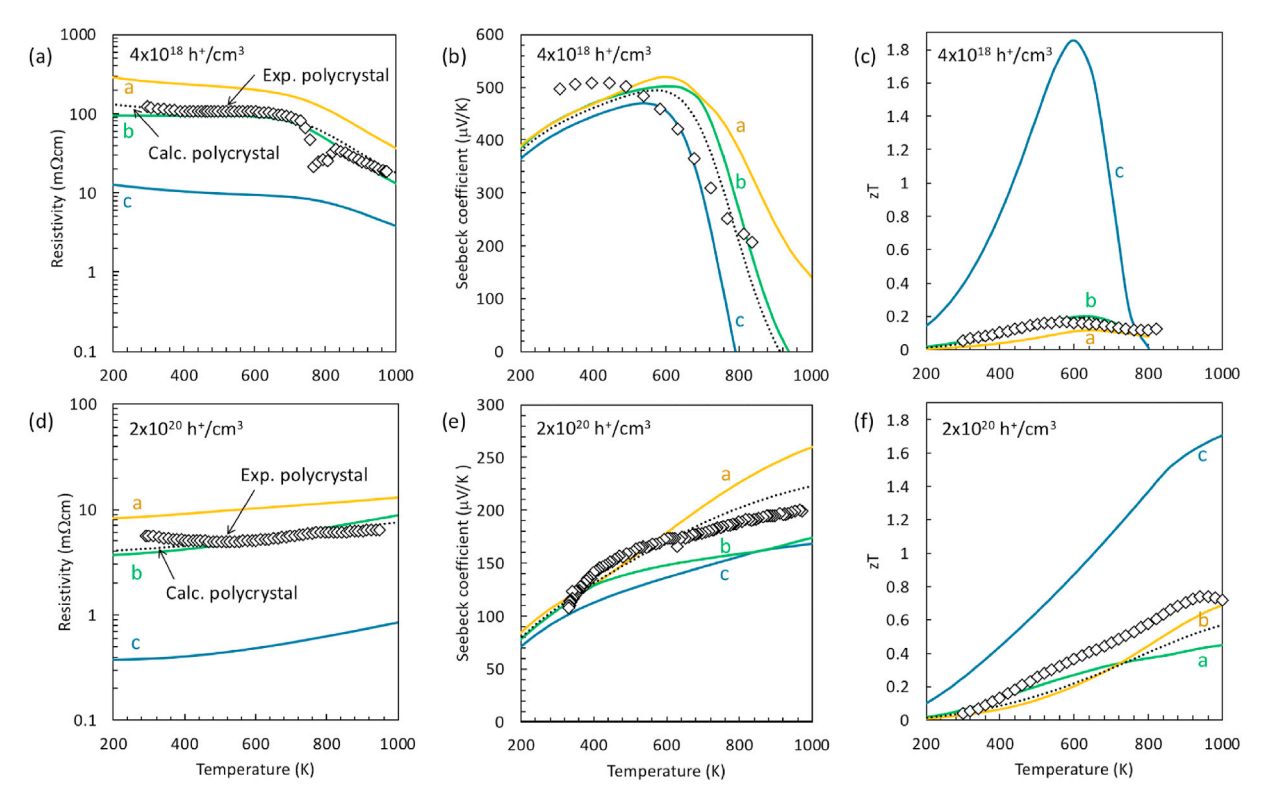
# 3.2. Predicted electronic transport properties

Fig. 3 shows the calculated electronic transport coefficients and zT of Ca<sub>5</sub>In<sub>2</sub>Sb<sub>6</sub> (solid and dotted curves) compared with experimental polycrystalline data from an undoped sample  $(n=4x10^{18}\ h^+/cm^3)$  and a Zn-doped sample  $(n=2x10^{20}\ h^+/cm^3)$ taken from Zevalkink et al. [17]. The transport along the three principle axes, as well as the directionally-average coefficients, were computed from the electronic band structure by solving the Boltzmann equation with energy-dependent relaxation times. The individual relaxation times for ionized impurity  $(\tau_{0,ii})$  and acoustic phonon  $(\tau_{0,ap})$  scattering were used as fitting parameters to ensure that the computed average resistivity matched the experimental resistivity of polycrystalline samples. Table 1 shows the value of  $\tau_0$ used to fit experimental results for the two scattering mechanisms. The polycrystalline average was taken as the average of the resistivities along the perpendicular axes. This average can be considered as an upper bound on the resistivity of the polycrystalline bulk, and thus may lead to slight overestimation of the single crystal resistivities [50].

In orthorhombic crystals, three coefficients ( $\rho_{xx}$ ,  $\rho_{yy}$ ,  $\rho_{zz}$ ) corresponding to transport along each of the principle axes (a, b, and c, respectively), are sufficient to fully describe the resistivity tensor,  $\rho_{ij}$ . Likewise for the Seebeck tensor,  $\alpha_{ij}$  [51] and the electronic thermal conductivities,  $\kappa_{e,ij}$  (the latter can be found in the supplemental information Figure S5). In Ca<sub>5</sub>In<sub>2</sub>Sb<sub>6</sub>, the predicted resistivity along the c-axis (parallel to the polyanionic chains) is found to be roughly an order of magnitude lower than the a- or b-axes, following the trend in conductivity effective mass described above. The ratio between the resistivity along the three directions remains largely constant as a function of temperature and Fermi level.

In contrast to the highly anisotropic electrical resistivity, the Seebeck coefficient varies by only 10-20% between the three principle axes at 200 K. Similar behavior has been noted in many anisotropic materials (e.g., SnSe [2], Bi<sub>2</sub>Te<sub>3</sub> [3] and GeAs [52]); the conductivity is often orders of magnitude more anisotropic than the Seebeck coefficient, thus leading to improved power factor along the high conductivity direction of the crystal. As shown by Parker et al. in ref. [39], the Seebeck coefficient will be isotropic as long as the band(s) can be modeled as a single parabolic band, and the scattering rate,  $\tau$ , is isotropic. This remains true regardless of the degree of band mass anisotropy. Our calculations assume by default that  $\tau$  is isotropic. Therefore, the predicted anisotropy in the Seebeck coefficient of Ca<sub>5</sub>In<sub>2</sub>Sb<sub>6</sub> arises due to deviations from parabolic band curvature and from the contributions of additional bands, especially from carrier excited to the conduction band. These contributions cause the Seebeck to become increasingly isotropic at high temperatures.

The predicted zT values shown in Fig. 3 were calculated using the experimental values of  $\kappa_l$  (~1.1 W/mK at 300 K - 0.7 W/mK at 1000 K) reported for the undoped polycrystalline sample in Ref. [12]. The predicted zT is highest in the c-direction for both p-type carrier concentration regimes, peaking at lower temperatures for n =  $10^{18}$  h<sup>+</sup>/cm<sup>3</sup>, due to activation of intrinsic carriers. While the directionally-averaged zT is predicted to be higher in doped samples (n =  $2 \times 10^{20}$  h<sup>+</sup>/cm<sup>3</sup>) than in undoped samples, the predicted zT along the c-direction is optimized at much lower carrier concentrations due to the lighter effective mass, peaking at 1.8 at 600 K. The zT predictions in Fig. 3(c) and (f) make two major assumptions



**Fig. 3.** The calculated directional (solid curves) and average (dotted curves) transport properties of  $Ca_5In_2Sb_6$  compared with experimental polycrystalline data (diamond symbols) from ref. [17]. Panels (a)—(c) show calculated data at  $4 \times 10^{18}$  h<sup>+</sup>/cm<sup>3</sup>, and panels (d) and (e) are at  $2 \times 10^{20}$  h<sup>+</sup>/cm<sup>3</sup>. The resistivity in the c-direction is predicted to be an order of magnitude lower than the a- and b-directions. This leads to higher predicted zT in the c-direction, assuming isotropic lattice thermal conductivity.

**Table 1** Values of  $\tau_0$  used to fit experimental results for ionized impurity scattering (II and acoustic phonon scattering (AP).

n [cm <sup>-3</sup> ]	$ au_0(\mathrm{II})$ [fs]	$ au_0(AP)$ [fs]
$\begin{array}{c} 4\times 10^{18} \\ 2\times 10^{20} \end{array}$	0.160 0.016	1600 55

that should not be taken for granted: 1) isotropic lattice thermal conductivity and 2) isotropic scattering of electronic carriers. Testing these assumptions experimentally is the focus of remainder of this study.

# 3.3. Evidence for isotropic lattice thermal conductivity

The anisotropy of the lattice thermal conductivity ( $\kappa_L$ ) of a crystal is primarily a function of the speed of sound tensor, which, in turn, is determined by the elastic tensor. McKinney et al. showed recently that anisotropic lattice thermal conductivity of a wide variety of materials can be reproduced reasonably well using only the computed elastic tensor [54]. In general, isotropic elastic constants lead to isotropic lattice thermal conductivity. The computed elastic tensor of Ca<sub>5</sub>ln<sub>2</sub>Sb<sub>6</sub> [53] was found to be only slightly anisotropic; the Young's modulus varies from 51 GPa in the x-direction to 64 GPa in the y-direction, suggesting that the ionic Ca–Sb bonds are as stiff as the polar-covalent In–Sb bonds forming the polyanionic backbone of the structure. From the elastic tensor of Ca<sub>5</sub>ln<sub>2</sub>Sb<sub>6</sub> we computed the speed of sound tensor, which is shown in Fig. 4(b). The speed of sound is nearly completely isotropic (see Table S1) which suggests that  $\kappa_L$  in Ca<sub>5</sub>ln<sub>2</sub>Sb<sub>6</sub> is likewise isotropic.

The large unit cell of Ca<sub>5</sub>In<sub>2</sub>Sb<sub>6</sub> (26 atoms per primitive cell) means that the optical modes may also play an important role in

heat transport. As can be seen from the computed phonon dispersion shown in Fig. S6, the velocity of the optical phonons in  $Ca_5In_2Sb_6$  are likewise nearly isotropic. Disparities between the a, b, and c directions ( $\Gamma$ -X,  $\Gamma$ -Y, and  $\Gamma$ -Z, respectively), are comparable to what we observe for acoustic velocities.

Lastly, we consider the possibility of anisotropic phonon scattering rates. The computed mode Grüneisen parameters of Ca<sub>5</sub>In<sub>2</sub>Sb<sub>6</sub> are shown in Fig. S6 and S7. Averaging the Grüneisen parameters along each principle axes yields slightly higher values for phonons propagating along the a- and b-directions (1.37 and 1.36, respectively) compared to the c-direction (1.27). These computed Grüneisen parameters are in excellent agreement with the experimental thermal expansion data. Fig. 4(c) shows the relative change in each lattice parameter as a function of temperature. The linear fits to the temperature dependent lattice parameters are shown in the supplemental information in Figure S8. The linear coefficients of thermal expansion of the a-axis are the highest  $(1.52 \times 10^{-5} K^{-1})$ , consistent with the higher Grüneisen parameter in that direction. The b- and c-axes are slightly lower  $(1.32 \times 10^{-5})$  and  $1.26 \times 10^{-5}$   $K^{-1}$ , respectively). However, the overall variation is less than 20%, suggesting that the anharmonic bonding character is comparable along the three primary directions, i.e., the ionic bonds and the covalent bonds are equally harmonic. This, combined with the isotropic speed of sound indicates that our earlier assumption of isotropic lattice thermal conductivity in Ca<sub>5</sub>In<sub>2</sub>Sb<sub>6</sub> was likely a reasonable one.

# 3.4. Structure and morphology of Ca<sub>5</sub>In<sub>2</sub>Sb<sub>6</sub> single crystals

Single crystals of Ca<sub>5</sub>In<sub>2</sub>Sb<sub>6</sub> were grown to verify the predicted electronic transport properties. Nominally undoped Ca<sub>5</sub>In<sub>2</sub>Sb<sub>6</sub> crystals were obtained from an In–Sb rich molten metal flux. Each

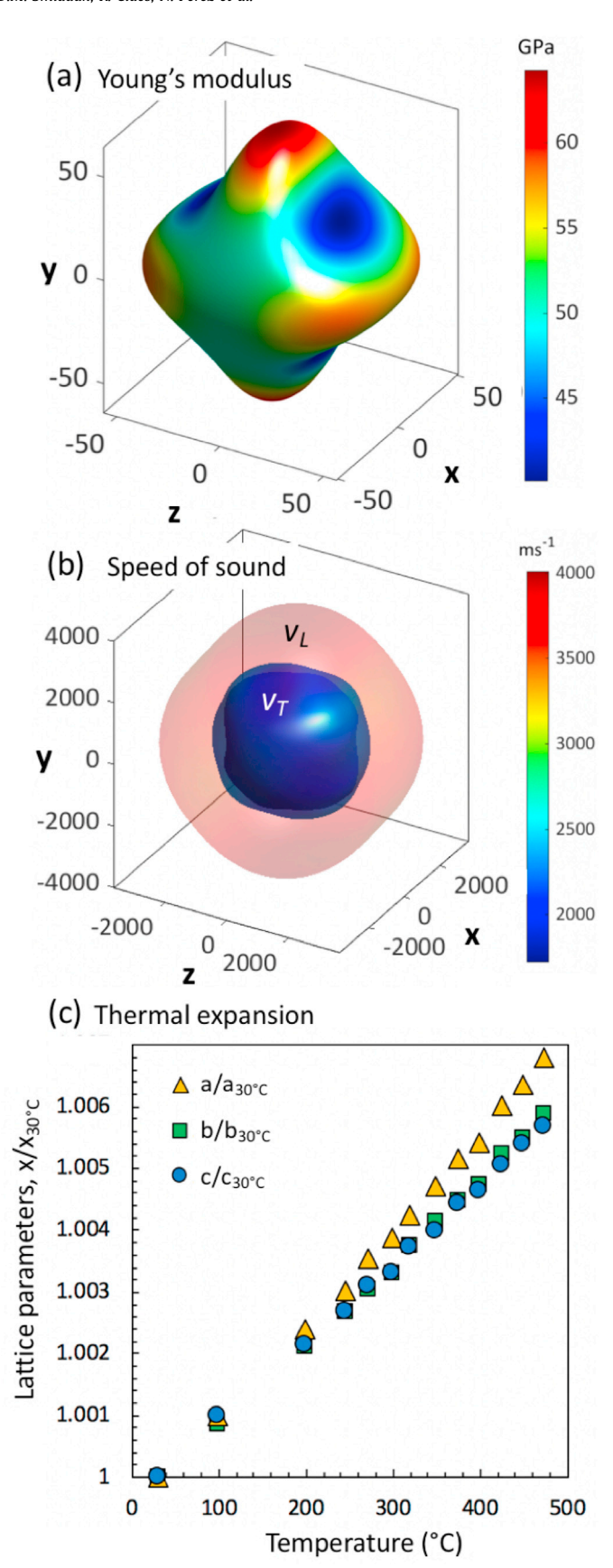


**Fig. 4.** Calculated (a) Young's modulus from ref [ [53]]. and (b) speed of sound as a function of orientation in  $Ca_5In_2Sb_6$  using elastic tensor available on MaterialsProject.org. (c) Lattice parameters of  $Ca_5In_2Sb_6$  measured as a function of temperature, normalized to room temperature. The linear CTE is proportional to the slope of each curve.

flux growth yielded a large number of small crystals, ranging from 100 µm to 5 mm in length. Representative SEM images of the grown Ca<sub>5</sub>In<sub>2</sub>Sb<sub>6</sub> single crystals are shown in Fig. 5(a). Crystal surfaces were flat and metallic in appearance, largely free of flux. The structure, stoichiometry, and orientation of the crystals were confirmed using SC-XRD. The crystals grew preferentially along the c-direction, [001], while the slowest growing direction was identified tentatively as the a-direction. [100]. The refined structure was consistent with the earlier reports by Cordier et al. [55]. Attempts were made to dope Ca<sub>5</sub>In<sub>2</sub>Sb<sub>6</sub> crystals by adding a small amount of Zn to the flux. Zn has been previously reported as an effective dopant for Ca<sub>5</sub>In<sub>2</sub>Sb<sub>6</sub> samples synthesized using a powder metallurgy approach [17]. However, instead of yielding Zn-doped Ca<sub>5</sub>In<sub>2</sub>Sb<sub>6</sub> crystals, the addition of Zn to the flux led – serendipitously – to the formation of an entirely new structure type, which we reported in Ref. [56].

# 3.5. Measurements of anisotropic electrical conductivity

The consequence of the highly anisotropic growth is that individual crystals can grow several millimeters along their preferred growth direction (c-direction) but only measured in the tens of microns in the perpendicular directions (a- and b-). A traditional four-probe method using manually-placed contacts could only be used to measure the resistivity parallel to the c-axis (blue symbols in Fig. 6(a)), but this method was impractical for measurements in the a- and b-directions. For this reason, we pursued microfabrication techniques whereby regularly-shaped micro-ribbons oriented either parallel or perpendicular to the c-axis were extracted from single crystals using a FIB milling technique. An example of this extraction process is shown in Fig. 5(b). A laser photolithography process was then used to apply sensors for transport measurements as shown in the schematic and SEM images in Fig. 5(c-d) [57]. The resistivity obtained from a micro-ribbon oriented perpendicular to the c-axis, shown as the green symbols in Fig. 6(a), was found to be 13–18x higher than the parallel direction. Note that the perpendicular micro-ribbon is concluded to be oriented along the a-direction based on SC-XRD characterization of different crystals from the same growth. The solid curves in Fig. 6(a) are the computed resistivity values along the principle axes at a carrier concentration of 10<sup>18</sup> h/cm<sup>3</sup>. Both the magnitude and anisotropy of the predicted resistivities agree well with the single crystal data.

The Hall coefficient was measured for the micro-ribbon in the temperature range of 220-300 K, yielding the p-type Hall carrier concentrations shown in the inset of Fig. 6(b). The carrier concentration was found to increase with increasing temperature, indicating that the crystal is an intrinsic semiconductor. The magnitude of the p-type carrier concentration was comparable to that of previously reported polycrystalline Ca<sub>5</sub>In<sub>2</sub>Sb<sub>6</sub> [12]. This similarity implies similar point defect densities and a narrow homogeneity range characteristic of a true line compound (at least with respect to excess In and Sb). The mobility of the microribbon (perp. to c) was calculated from the measured resistivity and Hall carrier concentration. We estimated the mobility of the macroscopic single crystal (parallel to c) from its resistivity by assuming it has the same carrier concentration. Both sets of single crystal data are compared to polycrystalline data from ref [12]. in Fig. 6(b). The c-direction mobility is significantly higher than the perpendicular direction and the polycrystalline sample, consistent with DFT. Anisotropic mobility can arise from either anisotropic conductivity effective mass,  $m^*$ , or relaxation time,  $\tau$ . Since the latter was not accounted for in our models, the excellent agreement between the measured and predicted anisotropy suggests that the effective mass - not the relaxation time - plays

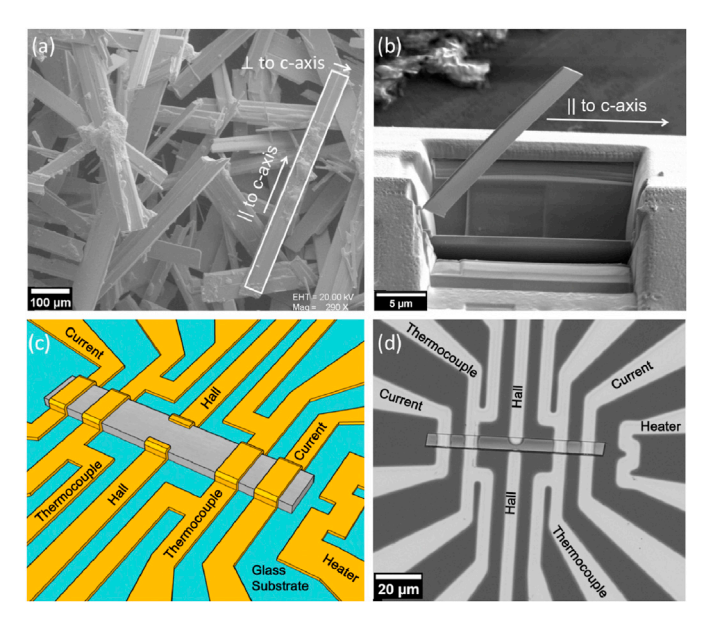


**Fig. 5.** (a) SEM image of  $Ca_5In_2Sb_6$  crystals obtained from flux growth and (b) an example of the FIB cutting process used to extract individual micro-ribbons from the crystals. (c) A 3D rendering of the circuit design shows the Cr–Au sensors (yellow) deposited on top of both the sample (grey) and the glass substrate (blue). (d) SEM image of a  $Ca_5In_2Sb_6$  micro-ribbon with final implementation of the circuit design.

the most important role in the anisotropic transport.

The ratio of the resistivity of Ca<sub>5</sub>In<sub>2</sub>Sb<sub>6</sub> measured parallel and perpendicular to the crystal growth direction is compared in Table 2 against other highly anisotropic single crystals. Both Ca<sub>5</sub>In<sub>2</sub>Sb<sub>6</sub> and CsBi<sub>4</sub>Te<sub>6</sub> contain 1D covalent chains, with parallel and perpendicular defined relative to the chain direction. For the layered compounds listed, parallel refers to in-plane and perpendicular is out-of-plane. This shows that Ca<sub>5</sub>In<sub>2</sub>Sb<sub>6</sub> possesses more anisotropic resistivity than the tetradymite compounds Bi<sub>2</sub>Te<sub>3</sub> and Sb<sub>2</sub>Te<sub>3</sub>, but less than the incredibly anisotropic CsBi<sub>4</sub>Te<sub>6</sub>. Mg<sub>3</sub>Sb<sub>2</sub> sometimes classified as a Zintl phase - exhibits relatively isotropic electronic transport (both experimentally and in DFT modeling [5]). Even though there are hundreds of thermoelectric materials with anisotropic structures, experimental data remains rare. In almost all cases, the "perpendicular" data is exceedingly difficult to obtain and it is often less reliable than the parallel measurements. This limitation is sometimes due to geometric constraints, as in the current study, or due to imperfections such as stacking faults in the crystals [61,62], or the use of a textured polycrystal instead of a single crystal, which introduces grain boundaries. This highlights the continued need for significant advances in both characterization techniques and crystal growth to help fill the gaps in our knowledge of anisotropic electronic transport in complex thermoelectric materials.

### 4. Conclusions

First principles modeling was used to show that the Zintl compound  ${\rm Ca}_5{\rm ln}_2{\rm Sb}_6$  has extremely anisotropic electrical resistivity due to light effective mass in the c-direction, parallel to its chain-like anionic sub-structure. The electrical resistivity and carrier concentration were measured on a single crystal micro-ribbon that was cut perpendicular to the c-direction. This data was compared against resistivity values collected on a single crystal parallel to the c-direction, yielding experimental confirmation of the predicted anisotropic electronic resistivity. A 13–18x increase in conductivity was observed parallel to the c-direction. DFT predicts a significantly

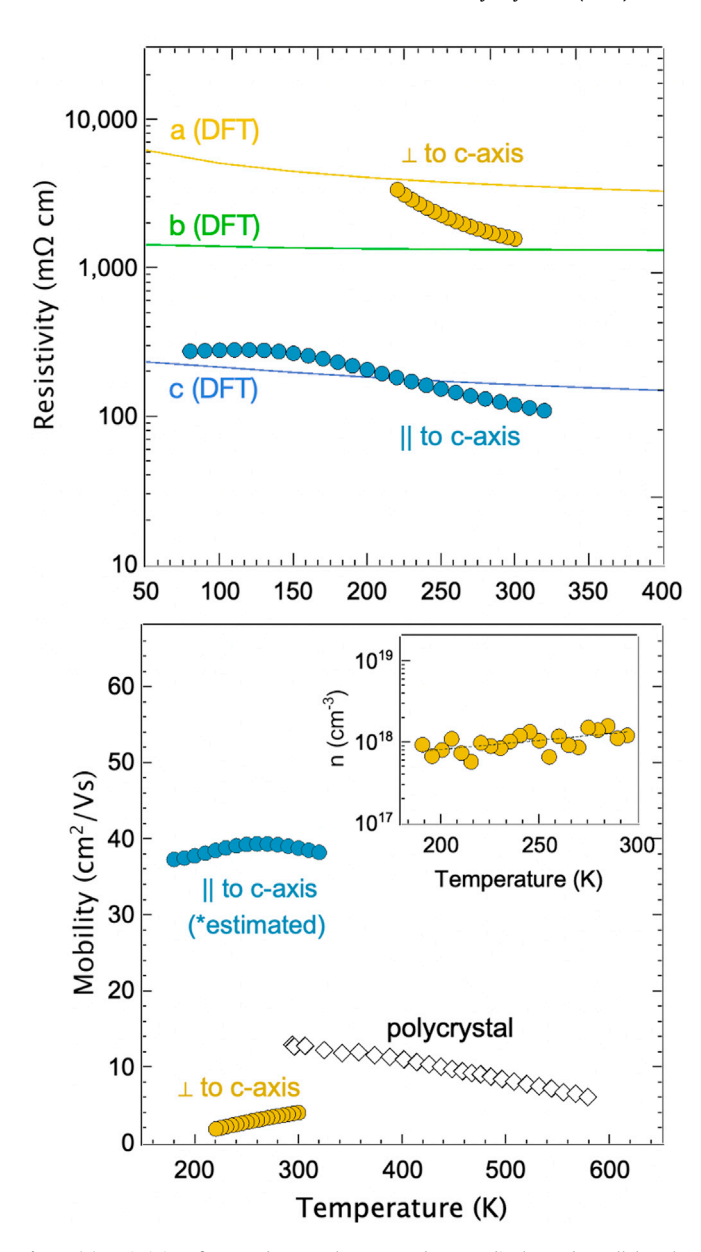


**Fig. 6.** (a) Resistivity of  $Ca_5In_2Sb_6$  crystals measured perpendicular and parallel to the c-direction. The solid curves are the computed resistivity at a carrier concentration of  $1 \times 10^{18}$  h/cm<sup>3</sup>. (b) Hall mobility of a polycrystalline samples compared with and single crystal data measured perpendicular and parallel to the c-direction. Inset of panel (b): Carrier concentration measured on micro-ribbon.

**Table 2** Ratio of electrical resistivity perpendicular  $(\rho_\perp)$  and parallel  $(\rho_\parallel)$  to the crystal growth direction at 200 and 300 K for selected bulk materials with quasi 1D or 2D crystal structures.

Compound	$\frac{ ho_{\perp}/ ho_{\parallel}}{200 \text{ K}}$	$\frac{\rho_{\perp}/\rho_{\parallel}}{300 \text{ K}}$	Ref.
$Ca_5In_2Sb_6$ (1D)	18.6	13.1	This work
$CsBi_4Te_6$ (1D)	127	86.7	[4]
$Bi_2Te_3$ (2D)	_	6.1	[3]
$Sb_2Te_3$ (2D)	_	1.8	[58]
$PbBi_4Te_7$ (2D)	5.7	4.3	[59]
$PbSb_2Te_4$ (2D)	12.0	10.1	[59]
$Mg_3Sb_2$ (2D)	0.50	0.49	[5]
SnSe (2D)	-	5.0	[60]

enhanced thermoelectric figure of merit parallel to the c-direction, assuming that the lattice thermal conductivity is isotropic. The latter assumption was supported by the calculated speed of sound tensor and the measured thermal expansion coefficients, both of which were found to be relatively isotropic. This study is the first experimental confirmation of quasi-1D electronic transport in a Zintl compound thermoelectric material. Further, it serves as proofof-concept for using micro-ribbons extracted from larger single crystals to evaluate thermoelectric properties in specific crystallographic directions. This process can potentially be applied to other compounds in the same manner to bridge the gap between experimental and computational evidence for anisotropic transport in Zintl compounds.

# Data availability

The raw data required to reproduce these findings cannot be shared at this time due to technical or time limitations. The processed data required to reproduce these findings cannot be shared at this time due to technical or time limitations.

# **Declaration of competing interest**

The authors declare that they have no known competing financial interests or personal relationships that could have appeared to influence the work reported in this paper.

#### **Acknowledgments**

Synthesis and characterization performed at Michigan State University were supported by the National Science Foundation (NSF) award number no. 1709158 and 2045122. Computational resources have been provided by the super computing facilities of the UCLouvain (CISM/UCL) and the Consortium des Équipements de Calcul Intensif (CÉCI), funded by the Fonds de la Recherche Scientifique de Belgique (F.R.S.- FNRS) under Grant No. 2.5020.11 and by the Walloon Region, as well as Communauté Française de Belgique grant ARC 18/23-093. D. S. would like to acknowledge Almut Pöhls for her heroic efforts using the FIB to cut and extract micro-ribbons and to Dr. Richard Staples and the Center of Crystallographic Research for crystallographic assistance.

# Appendix A. Supplementary data

Supplementary data to this article can be found online at https://doi.org/10.1016/j.mtphys.2021.100597.

# References

- [1] L.E. Bell, Cooling, heating, generating power, and recovering waste heat with
- thermoelectric systems, Science 321 (2008) 1457–1461.
  [2] L.D. Zhao, S.H. Lo, Y. Zhang, H. Sun, G. Tan, C. Uher, C. Wolverton, V.P. Dravid, M.G. Kanatzidis, Ultralow thermal conductivity and high thermoelectric figure of merit in SnSe crystals, Nature 508 (2014) 373-377.
- [3] J.H. Dennis, Anisotropy of thermoelectric power in bismuth telluride, in: MIT Research Lab. Electronics, Technical Report, 1961.
- [4] D.-Y. Chung, S. Mahanti, W. Chen, C. Uher, M. Kanatzidis, Anisotropy in thermoelectric properties of CsBi<sub>4</sub>Te<sub>6</sub>, Mater. Res. Soc. Symp. Proc. 793 (2004)
- [5] J. Xin, G. Li, G. Auffermann, H. Borrmann, W. Schnelle, J. Gooth, X. Zhao, T. Zhu, C. Felser, C. Fu, Growth and transport properties of  $Mg_3X_2$  (X = Sb, Bi) single crystals, Mater. Today Phys. 7 (2018) 61–68.
- S.M. Kauzlarich, Chemistry, Structure, and Bonding of Zintl Phases and Ions, VCH Publishers, 1996.
- [7] E.S. Toberer, A.F. May, G.J. Snyder, Zintl chemistry for designing high efficiency thermoelectric materials, Chem. Mater. 22 (2010) 624-634.
- [8] E.S. Toberer, C.A. Catherine, S.R. Brown, T. Ikeda, A.F. May, S.M. Kauzlarich, G.J. Snyder, Traversing the metal-insulator transition in a Zintl phase: rational enhancement of thermoelectric efficiency in Yb<sub>14</sub>Mn<sub>1-x</sub>Al<sub>x</sub>Sb<sub>11</sub>, Adv. Funct. Mater. 18 (2008) 2795-2800.

- [9] J. Shuai, H. Geng, Y. Lan, Z. Zhu, C. Wang, Z. Liu, J. Bao, C.-W. Chu, J. Sui, Z. Ren, Higher thermoelectric performance of Zintl phases  $(Eu_{0.5}Yb_{0.5})_{1-x}Ca_xMg_2Bi_2$ by band engineering and strain fluctuation, Proc. Natl. Acad. Sci. Unit. States Am, 113 (2016) E4125–E4132.
- [10] B.R. Ortiz, P. Gorai, V. Stevanovi, E.S. Toberer, Thermoelectric performance and defect chemistry in n-type Zintl KGaSb<sub>4</sub>, Chem. Mater. 29 (2017) 4523-4534.
- [11] U. Aydemir, A. Zevalkink, A. Ormeci, Z.M. Gibbs, S. Bux, G.J. Snyder, Thermoelectric enhancement in Baga<sub>2</sub>Sb<sub>2</sub> by Zn doping, Chem. Mater. 27 (2015) 1622-1630
- [12] A. Zevalkink, G. Pomrehn, S. Johnson, J. Swallow, Z. Gibbs, G. Snyder, Influence of the triel elements (M= Al, Ga, in) on the transport properties of Ca<sub>5</sub>M<sub>2</sub>Sb<sub>6</sub> Zintl compounds, Chem. Mater. 24 (2012) 2091–2098.
- [13] J. Sun, D.J. Singh, Thermoelectric properties of AMg<sub>2</sub>X<sub>2</sub>, AZn<sub>2</sub>Sb<sub>2</sub> (A = Ca, Sr, Ba; X = Sb, Bi), and  $Ba_2ZnX_2$  (X = Sb, Bi) Zintl compounds, J. Mater. Chem. 5 (2017) 8499-8509.
- [14] B. Xu, R. Li, G. Yu, S. Ma, Y. Wang, Y. Wang, L. Yi, The relation between the electronic structure and thermoelectric properties for Zintl compounds Mg<sub>3</sub>Sb<sub>2</sub>, J. Phys. Soc. Jpn. 86 (2017), 024601.
- [15] G. Yang, G. Zhang, C. Wang, Y. Wang, The unusual chemical bonding and thermoelectric properties of a new type Zintl phase compounds Ba<sub>3</sub>Al<sub>2</sub>As<sub>4</sub>, Solid State Commun. 237–238 (2016) 28–33.
  [16] R.A. Ribeiro, M.A. Avila, Single crystal flux growths of thermoelectric mate-
- rials, Phil. Mag. 92 (2012) 2492–2507.
- A. Zevalkink, J. Swallow, G.J. Snyder, Thermoelectric properties of Zn-doped Ca<sub>5</sub>In<sub>2</sub>Sb<sub>6</sub>, Dalton Trans. 42 (2013) 9713–9719.
- [18] P. Canfield, T. Kong, U. Kaluarachchi, N. Jo, Use of frit-disc crucibles for routine and exploratory solution growth of single crystalline samples, Philos. Mag. A 96 (2016) 84-92.
- [19] Bruker AXS Inc, SAINT (2014).
- [20] G.M. Sheldrick, SHELXT integrated space-group and crystal-structure determination, Acta Crystallogr. A 71 (2015) 3-8.
- O. Dolomanov, L. Bourhis, R. Gildea, J. Howard, H. Puschmann, OLEX2: a complete structure solution, refinement and analysis program, J. Appl. Crystallogr. 42 (2009) 339-341.
- [22] G.M. Sheldrick, Crystal structure refinement with SHELXL, Acta Crystallogr. C 71 (2015) 3-8.
- [23] Lasi Integrated circuit design for windows. https://lasihomesite.com/index. htm. 2004-2018.
- [24] D.M. Smiadak, Single Crystal Growth and Characterization of Zintl Phase Thermoelectric Compounds, Ph.D. thesis, Michigan State University, 2020.
- [25] J. Hafner, Materials simulations using VASPa quantum perspective to materials science, Comput. Phys. Commun. 177 (2007) 6-13.
- [26] J.P. Perdew, K. Burke, M. Ernzerhof, Generalized gradient approximation made simple, Phys. Rev. Lett. 77 (1996) 3865.
- [27] G. Kresse, J. Furthmüller, Efficiency of ab-initio total energy calculations for metals and semiconductors using a plane-wave basis set, Comput. Mater. Sci. 6 (1996) 15-50.
- [28] G. Kresse, J. Furthmüller, Efficient iterative schemes for ab initio total-energy calculations using a plane-wave basis set, Phys. Rev. B 54 (1996) 11169.
- [29] D. Waroquiers, A. Lherbier, A. Miglio, M. Stankovski, S. Poncé, M.J.T. Oliveira, M. Giantomassi, G.-M. Rignanese, X. Gonze, Band widths and gaps from the Tran-Blaha functional: comparison with many-body perturbation theory, Phys. Rev. B 87 (2013): 075121.
- [30] G.K. Madsen, D.J. Singh, Boltz TraP. A code for calculating band-structure dependent quantities, Comput. Phys. Commun. 175 (2006) 67-71.
- S.P. Ong, W.D. Richards, A. Jain, G. Hautier, M. Kocher, S. Cholia, D. Gunter, V.L. Chevrier, K.A. Persson, G. Ceder, Python Materials Genomics (pymatgen): a robust, open-source python library for materials analysis, Comput. Mater. Sci. 68 (2013) 314-319.
- [32] B.M. A. Electron Transport Phenomena in Semiconductors, World scientific.
- [33] X. Gonze, et al., Recent developments in the ABINIT software package, Comput. Phys. Commun. 205 (2016) 106-131.
- [34] X. Gonze, et al., ABINIT: first-principles approach to material and nanosystem properties, Comput. Phys. Commun. 180 (2009) 2582-2615, 40 YEARS OF CPC: A celebratory issue focused on quality software for high performance, grid and novel computing architectures.
- [35] A. Zevalkink, U. Aydemir, G.J. Snyder, in: C. Uher (Ed.), Chain-forming A<sub>3</sub>MPn<sub>3</sub> and A5M2Pn6 Zintl Phases in CRC Handbook of Thermoelectrics, CRC Press,
- [36] G. Hautier, A. Miglio, D. Waroquiers, G. Rignanese, X. Gonze, How does chemistry influence electron effective mass in oxides? A high-throughput computational analysis, Chem. Mater. 26 (2014): 54475458.
- [37] G. Hautier, A. Miglio, G. Ceder, G.-M. Rignanese, X. Gonze, Identification and design principles of low hole effective mass p-type transparent conducting oxides, Nat. Commun. 4 (2013) 2292.
- [38] G. Brunin, F. Ricci, V.-A. Ha, G.-M. Rignanese, G. Hautier, Transparent conducting materials discovery using high-throughput computing, npj Comput. Mater. 5 (2019).
- [39] D.S. Parker, A.F. May, D.J. Singh, Benefits of carrier-pocket anisotropy to thermoelectric performance: the case of p-type AgBiSe<sub>2</sub>, Phys. Rev. Applied 3 (2015): 064003.
- [40] S. Ohno, A. Zevalkink, Y. Takagiwa, S.K. Bux, G.J. Snyder, Thermoelectric properties of the Yb<sub>9</sub>Mn<sub>4,2-x</sub>Zn<sub>x</sub>Sb<sub>9</sub> solid solutions, J. Mater. Chem. 2 (2014)

- [41] S. Chanakian, U. Aydemir, A. Zevalkink, Z.M. Gibbs, J.P. Fleurial, S. Bux, G.I. Snyder, High temperature thermoelectric properties of Zn-doped Eu<sub>5</sub>In<sub>2</sub>Sb<sub>6</sub>, J. Mater. Chem. C 3 (2015) 10518–10524.
- [42] Bux, S. K.; Zevalkink, A.; Janka, O.; Uhl, D.; Kauzlarich, S.; Snyder, G. J.; Fleurial, I. P. Glass-like lattice thermal conductivity and high thermoelectric efficiency in Yb<sub>9</sub>Mn<sub>4.2</sub>Sb<sub>9</sub>. J. Mater. Chem. 214, 2, 215–220.
- [43] E.S. Toberer, A.F. May, B.C. Melot, E. Flage-Larsen, G.J. Snyder, Electronic structure and transport in thermoelectric compounds  $AZn_2Sb_2$  (A = Sr, Ca, Yb, Eu). Dalton Trans. 39 (2010) 1046-1054.
- [44] A. Zevalkink, S. Chanakian, U. Aydemir, A. Ormeci, G. Pomrehn, S. Bux, J.P. Fleurial, G.J. Snyder, Thermoelectric properties and electronic structure of the Zintl phase  $Sr_5In_2Sb_6$  and the  $Ca_{5-x}Sr_xIn_2Sb_6$  solid solution, J. Phys. Condens. Matter 27 (2015): 015801.
- [45] A.F. May, G.J. Snyder, In Introduction to modeling thermoelectric transport at high temperatures, in: D.M. Rowe (Ed.). Thermoelectrics and its Energy Harvesting, vol. 1, CRC Press, 2012.
- [46] A. Zevalkink, E.S. Toberer, W.G. Zeier, E. Flage-Larsen, G.J. Snyder, Ca<sub>3</sub>AlSb<sub>3</sub>: an inexpensive, non-toxic thermoelectric material for waste heat recovery, Energy Environ. Sci. 4 (2011) 510–518.
- [47] F. Meng, S. Sun, J. Ma, C. Chronister, J. He, W. Li, Anisotropic thermoelectric figure-of-merit in Mg3Sb2, Mater. Today Phys. 13 (2020): 100217.

  [48] J. Xin, G. Li, G. Auffermann, H. Borrmann, W. Schnelle, J. Gooth, X. Zhao, T. Zhu,
- C. Felser, C. Fu, Growth and transport properties of Mg3X2 (X= Sb, Bi) single crystals, Mater. Today Phys. 7 (2018) 61–68.
- [49] J. Zhang, L. Song, M. Sist, K. Tolborg, B.B. Iversen, Chemical bonding origin of the unexpected isotropic physical properties in thermoelectric Mg3Sb2 and related materials, Nat. Commun. 9 (2018) 4716.
- [50] Z. Hashin, S. Shtrikman, Conductivity of polycrystals, Phys. Rev. 130 (1963) 129-133
- [51] R.E. Newnham, Properties of Materials: Anisotropy, Symmetry, Structure, Oxford University Press, 2005.
- [52] K. Lee, S. Kamali, T. Ericsson, M. Bellard, K. Kovnir, GeAs: highly anisotropic

- van der Waals thermoelectric material, Chem. Mater. 28 (2016) 2776–2785. [53] M. de Jong, W. Chen, A.J. Thomas Angsten, R. Notestine, A. Gamst, M. Sluiter, C.K. Ande, S. van der Zwaag, J.J. Plata, C. Toher, S. Curtarolo, G. Ceder,
- K.A. Persson, M. Asta, Charting the complete elastic properties of inorganic crystalline compounds, Sci. Data 2 (2015): 150009.
- [54] R. McKinney, P. Gorai, E.S. Toberer, V. Stevanovic, Rapid prediction of anisotropic lattice thermal conductivity: application to layered materials, Chem. Mater. 31 (2019) 2048-2057.
- G. Cordier, H. Schäfer, M. Stelter, Perantimonidogallate und -indate: zur Kenntnis von Ca<sub>5</sub>Ga<sub>2</sub>Sb<sub>6</sub>, Ca<sub>5</sub>In<sub>2</sub>Sb<sub>6</sub> und Sr<sub>5</sub>In<sub>2</sub>Sb<sub>6</sub>, Z. Naturforsch. 40 (1985) 5-8.
- [56] D.M. Smiadak, S. Baranets, M. Rylko, M. Marshall, M. Calderón-Cueva, S. Bobey, A. Zevalkink, Single crystal growth and characterization of new Zintl phase Ca<sub>9</sub>Zn<sub>3.1</sub>In<sub>0.9</sub>Sb<sub>9</sub>, J. Solid State Chem. 296 (2021): 121947.
- [57] J. Gooth, A. Niemann, T. Meng, A. Grushin, K. Landsteiner, B. Gotsmann, F. Menges, M. Schmidt, C. Shekhar, V. Suss, R. Hune, B. Rellinghaus, C. Felser, B. Yan, K. Nielsch, Experimental signatures of the mixed axial-gravitational anomaly in the Weyl semimetal NbP, Nature 547 (2017) 324–327.
- [58] L. Ivanova, Y. Granatkina, Y. Sidorov, Electrical properties of antimony telluride single crystals doped with selenium and bismuth, Neorg. Mater. 35 (1999) 44-52
- [59] L. Shelimova, T. Svechnikova, P. Konstantinov, O. Karpinskii, E. Avilov, M. Kretova, V. Zemskov, Anisotropic thermoelectric properties of the layered compounds PbSb<sub>2</sub>Te<sub>4</sub> and PbBi<sub>4</sub>Te<sub>7</sub>, Inorg. Mater. 43 (2007) 125–131.
- L. Zhao, S. Lo, Y. Zhang, H. Sun, G. Tan, C. Uher, C. Wolverton, V. Dravid, M. Kanatzidis, Ultralow thermal conductivity and high thermoelectric figure of merit in SnSe crystals, Nature 508 (2014) 373–377.
- L. Seixas, L.B. Abdalla, T.M. Schmidt, A. Fazzio, R.H. Miwa, Topological states
- ruled by stacking faults in Bi<sub>2</sub>Se<sub>3</sub> and Bi<sub>2</sub>Te<sub>3</sub>, J. Appl. Phys. 113 (2013): 023705. [62] D. Ibrahim, J.-B. Vaney, S. Sassi, C. Candolfi, V. Ohorodniichuk, P. Levinsky, C. Semprimoschnig, A. Dauscher, B. Lenoir, Reinvestigation of the thermal properties of single-crystalline SnSe, Appl. Phys. Lett. 110 (2017): 032103.